

# Progress in Warm Dense Matter and Planetary Physics

Winfried Lorenzen, Andreas Becker, and Ronald Redmer

**Abstract** We give an introduction into the method of quantum molecular dynamics simulations which combines density functional theory with classical molecular dynamics. This method has demonstrated its predictive power in determining the thermophysical properties of matter under extreme conditions as found, e.g., in astrophysical objects like giant planets and brown dwarfs. Such extreme states of matter can also be probed by state-of-the-art shock wave experiments in the laboratory. We give exemplary ab initio results for the behavior of the simplest and most abundant elements hydrogen and helium under extreme conditions. In addition, we also show results for more complex molecular systems such as water. The light elements H and He, the hydrides of C ( $\text{CH}_4$ ), N ( $\text{NH}_3$ ), and O ( $\text{H}_2\text{O}$ ) and, in particular, mixtures of these systems have rich high-pressure phase diagrams which are important for the structure, evolution and magnetic field of gas giant planets like Jupiter and ice giant planets like Neptune. Finally, we describe the impact of these results on the design of advanced interior, evolution, and dynamo models and give exemplary results for solar and extrasolar giant planets.

## 1 Introduction

### 1.1 Warm Dense Matter

The properties of warm dense matter (WDM) are of lively interest [1–3]. As an intermediate state between cold condensed matter and hot plasmas, WDM is

---

W. Lorenzen • A. Becker (✉) • R. Redmer  
Institute of Physics, University of Rostock, 18051 Rostock, Germany  
e-mail: [winfried.lorenzen@uni-rostock.de](mailto:winfried.lorenzen@uni-rostock.de); [andreas.becker@uni-rostock.de](mailto:andreas.becker@uni-rostock.de);  
[ronald.redmer@uni-rostock.de](mailto:ronald.redmer@uni-rostock.de)

characterized by high densities as typical for condensed matter and temperatures of several eV ( $1 \text{ eV} \hat{=} 11,604.5 \text{ K}$ ). Partial ionization, strong correlations and quantum effects are important under such conditions so that WDM is a perfect test case for new concepts of many-particle theory. On the other hand, the implementation of new experimental high-pressure platforms that launch strong shock waves by using, e.g., high-power lasers, gas guns, pulsed power or chemical explosions, and the availability of intense x-ray sources, in particular of free electron lasers (FEL), allows to probe and diagnose WDM states with better and better accuracy [4].

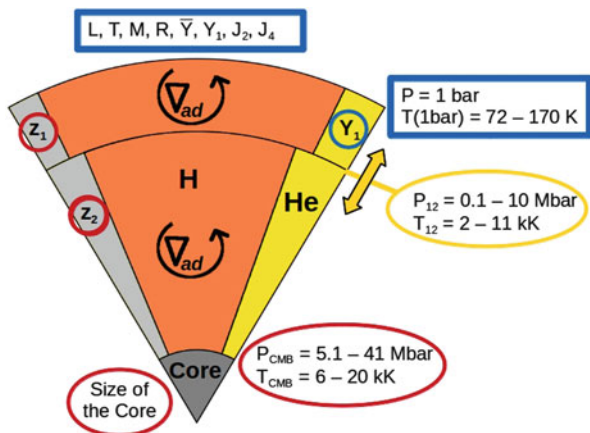
The strongest and perhaps most sustaining influence on WDM research originates from problems in astrophysics [5, 6]. For instance, the interior of giant planets (GPs) such as Jupiter and Saturn is in WDM states [7, 8]. The detection of a great number of extrasolar planets (exoplanets) since 1995 has boosted the interest in WDM as well [9–12]. The formation, evolution, interior structure, and magnetic field configuration of planets is intimately connected with the equation of state (EOS), the phase diagram, the transport and optical properties of planetary materials at extreme conditions of pressure and temperature, i.e. in WDM states. Interesting phenomena such as demixing [13, 14] and nonmetal-to-metal transitions [15, 16] are of fundamental interest in this context but also new and exotic phases such as proton conductors might be important in the deep interior of, e.g., Neptune-like planets [17–19].

An adequate theoretical treatment of WDM faces enormous computational challenges which are caused by inherent strong correlation and quantum effects. This prevents the application of methods of perturbation theory using effective pair potentials or of corresponding cross sections. Therefore, and also due to the huge progress in computational power, *ab initio* simulation techniques have been developed. Both Path Integral Monte Carlo (PIMC) simulations and Quantum Molecular Dynamics simulations, based on density functional theory (DFT-MD), have demonstrated their ability to determine thermophysical properties of WDM accurately.

The key elements of PIMC simulations are the representation of the density matrix via a path-integral and the evaluation of the corresponding integrals via Monte Carlo methods; for details, see [20]. In DFT-MD simulations, the electronic structure is determined via finite-temperature density functional theory at every timestep of a classical molecular dynamics simulation for the ions; see e.g. [21, 22].

In this paper we give a brief introduction into the DFT-MD method and present exemplary results for the most abundant planetary materials, especially hydrogen and helium, covering equation of state (EOS) data, the phase diagram, and the electrical conductivity. We discuss the impact of these *ab initio* data on state-of-the-art models of planetary interiors, evolution scenarios, and magnetic fields configurations.

**Fig. 1** Standard three-layer structure model assumed for the solar GPs with observational constraints (blue), variable parameters (yellow) and results from the modeling procedure (red)



## 1.2 Giant Planets in the Solar System

Our solar system consists of four rocky planets (Mercury, Venus, Earth, and Mars) and four GPs (Jupiter, Saturn, Uranus, and Neptune). In this paper we focus on the behavior of the lightest elements hydrogen and helium, their mixtures, and of hydrides such as water under conditions as relevant for the interior of GPs. Figure 1 gives a schematic representation of the interiors of the solar GPs within a standard three-layer model [7]: a central rocky core is surrounded by two fluid envelopes which are assumed to be fully convective so that the pressure-temperature profile follows an adiabat. The mass fractions of hydrogen ( $X$ ), helium ( $Y$ ), and of all heavier elements (i.e. *metals*,  $Z$ ) can be different in each layer. From observations we know for the solar GPs the mass  $M$ , radius  $R$ , surface pressure  $P(R)$  and temperature  $T(R)$ , the mean helium mass fraction  $\bar{Y}$  and the atmospheric helium mass fraction  $Y_1$ , the atmospheric metallicity  $Z_1$ , the period of rotation, the lowest-order gravitational moments  $J_{2i}$ , the age of the planet and its luminosity  $L$ . These *observational constraints* are used to infer details about the interior structure, see Sect. 4.1. The interior of the solar GPs is in WDM states, see Fig. 1: the boundary between the fluid envelopes is at about  $P_{12} \sim (0.1 - 10)$  Mbar and  $T_{12} \sim (2,000 - 11,000)$  K, while the core-mantle boundary is predicted at about  $P_{\text{CMB}} \sim (5 - 40)$  Mbar and  $T_{\text{CMB}} \sim (6,000 - 20,000)$  K. Therefore, the thermophysical properties of WDM are an essential ingredient in planetary physics studies. Some fundamental problems in this context are

- The number and composition of the layers (e.g. less or more than three?),
- The physical origin of the layer boundaries (e.g. due to *metallization* of hydrogen or due to *demixing* of helium from hydrogen?),
- Their stability and location inside the planet (e.g. does vertical mass transport and/or core erosion occur?),

- The size and thermodynamic state of the core (e.g. is there a core at all and, if yes, is it solid or liquid?),
- The derivation of mass-radius relations for GPs dependent on their composition,
- The origin of the planetary dynamo and the shape of the magnetic field (i.e. dipolar field or higher multipole moments, axisymmetric or tilted?),
- The understanding of the formation process of GPs (i.e. *core accretion* or *disk instability*?),
- The presence of internal heat sources such as helium settling, and the heat transport mechanisms (i.e. convection only or semi-convection?).

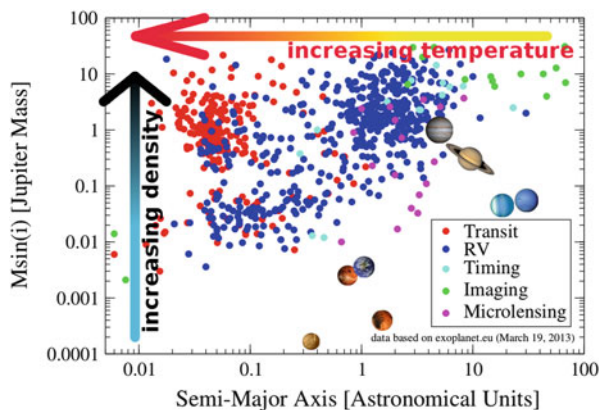
### 1.3 Extrasolar Giant Planets

The number of extrasolar GPs is rapidly increasing, with already hundreds of detected planets around other stars [9–12]. Therefore, planetary physics has been revolutionized since the discovery of the first exoplanet around a solar-like star in 1995 (51 Pegasi [23]). The most successful observational techniques are the radial velocity (RV) and the transit method. The first one investigates variations of spectral lines emitted by the star via the Doppler effect. These change periodically due to the star's motion around the common center-of-mass if the star has one or more planetary companions. The RV method gives information on the minimum mass of the accompanying planet. The transit method yields the mean radius of the planet eclipsing its host star since the decrease of the apparent stellar flux is proportional to the size of the planet, i.e.  $\sim R_p^2$ . Most important in this context is that the CoRoT [24] and Kepler [25] missions were designed in order to detect a large number of transiting planets, among them hopefully the first Earth-like planet in the habitable zone of its parent star. Today, the sample size of exoplanets with known masses and radii for which their bulk density can be derived is exceeding 200 [26, 27]. Based on this data, new models for their composition and interior structure, their formation and evolution can be made which are in many aspects very different from the assumptions that have been proposed for the solar GPs until 1995. Other methods to detect exoplanets are pulsar timing, direct imaging, and microlensing, see [9, 12]. Further substantial progress in planetary physics is expected since the number of exoplanets and, therefore, the sample size, is rapidly increasing.

All known exoplanets detected by these methods (color coded) are shown in Fig. 2 together with the solar system planets. We display their mass with respect to the orbital distance to their host stars (semi-major axis). Since transiting probability and frequency decrease with increasing distance from the star, most of the detected transiting planets are very close to their host stars. On the other hand, large planetary masses lead to stronger Doppler shifts in the star spectrum and, thus, to a better detectability so that most of the detected RV planets so far have Jupiter-like masses.

The two big arrows in Fig. 2 indicate that the closer a planet orbits its host star the hotter is its interior. Simultaneously, the density in the interior of a planet increases

**Fig. 2** The mass of exoplanets versus their semi-major axis (data taken from [28]). The color code represents the detection method: *dark blue* – RV method, *red* – transit method, *light blue* – pulsar timing, *green* – imaging, *magenta* – microlensing. The solar system planets are shown for comparison (size not true to scale)

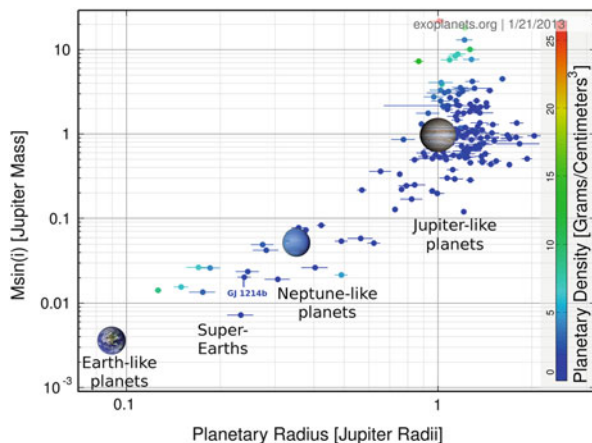


with the total mass of the planet. Therefore, the solar GPs and the rapidly growing sample of exoplanets represent a perfect laboratory to scan the density-temperature plane and, therefore, to study correlation and quantum effects as inherent in WDM.

As of April 2013, there are about 850 confirmed exoplanet candidates. A further 2,000 candidates were detected by the Kepler mission [25, 29]. Their statistics indicates that most exoplanets are of Neptune-size or smaller which leads to a classification depending on their mass and radius (and hence their density) in Earth-like, Neptune-like, Jupiter-like planets and Super-Earths. The latter planetary class has no representative in the solar system, an example is GJ 1214b [30, 31]. Another interesting planet is Kepler 22 with a radius of  $2.4 R_E$  ( $1 R_E = 6,378 \text{ km}$ ) and a mass of  $10\text{--}35 M_E$  ( $1 M_E = 5.974 \cdot 10^{24} \text{ kg}$ ) – the first detected exoplanet in the habitable zone of its host star [32]. The Kepler 11 system [33] consists of at least six transiting planets, the inner five have radii of few Earth radii and masses between that of Earth and Neptune, i.e.  $(1\text{--}18) M_E$ . Their mean densities imply that planets b and c are Super-Earths and d-f represent perhaps small gaseous planets, i.e. planets with no analog in our solar system. The region of detected exoplanets has been extended recently to objects even smaller than Mercury: the Kepler 37 system [34] consists of three transiting planets, the innermost having a radius of only  $\sim 0.3 R_E$  and thus its size is similar to that of the Moon. The first exoplanet observed by direct imaging is Formalhaut b, a Jupiter-like planet orbiting its host star in an eccentric orbit with a mean distance of 115 AU within a dust ring [35]. A catalogue of confirmed exoplanets can be found at [28]. The classification of exoplanets is shown in Fig. 3 by means of a mass-radius relation.

Some points are important for the future development of this field. First, the rapidly growing number of exoplanets will have a strong impact on astrophysics and, simultaneously, will initiate further interest in WDM research. Second, new high-pressure platforms such as NIF and diagnostic methods implemented at FELs will lead to breakthroughs in dense plasma experimental research. Third, the ongoing increase of computing power will promote the development and application

**Fig. 3** Classification of exoplanets with respect to Earth-like, Neptune-like and Jupiter-like planets and Super-Earths (e.g. GJ 1214b) [36]



of ab initio methods in WDM research. These trends will advance a much stronger overlap and interplay between plasma, planetary, and computational physics in the future.

## 2 DFT-MD Simulations

As outlined in the introduction, DFT-MD simulations combine quantum mechanical DFT calculations for the electrons with a classical MD simulation for the ions. The basic workflow is shown in Fig. 4, and the constituents, especially the DFT part, are explained in the following sections. This method has first been applied to plasma physics and WDM in the 1990s [40, 41]. Other chapters in this book deal with special aspects of this method. New developments for higher accuracy and predictability (e.g. deriving better XC functionals) and more efficient methods to solve the Kohn-Sham equations (see Sect. 2.1, e.g. using plane-waves [22] or localized orbitals [42] as basis sets) will trigger future progress in this area.

### 2.1 Kohn-Sham Equations

The solution of the many-particle Schrödinger equation requires an enormous amount of dimensions which is not feasible for more than a few ( $<10$ ) electrons. This problem can be circumvented by density functional theory, which deals with the quantum mechanical description of electrons in an external potential. It is based on the theorems of Hohenberg and Kohn [43] which state:

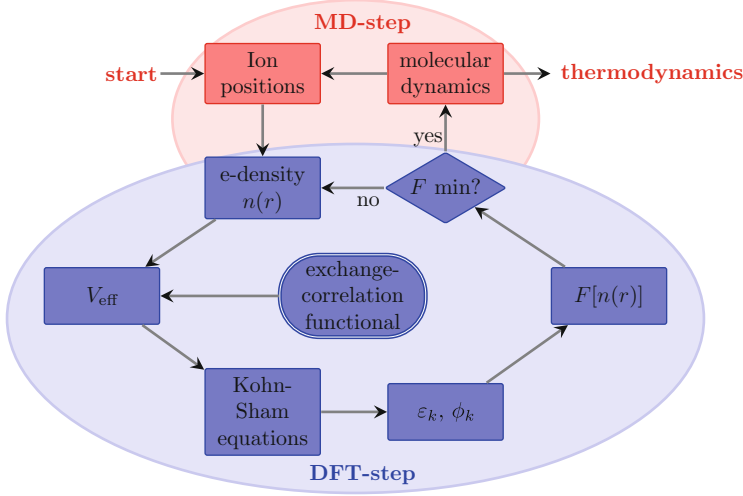


**Fig. 4** DFT-MD workflow as implemented in VASP [22, 37–39]. The central part of the method is the DFT calculation (blue) which is performed for each MD step (red). Basic input for the DFT calculation is the XC functional

1. If two (electron) systems with an external potential  $v_1(\mathbf{r})$  and  $v_2(\mathbf{r})$  have the same ground state density  $n(\mathbf{r})$ , then the potentials can only differ by a constant.
2. The density functional  $E[n(\mathbf{r})]$  has its minimum at the ground state density.

This was generalized to finite temperatures by Mermin [44] where a functional  $\Omega[n(\mathbf{r})]$ , corresponding to the grand potential or, more relevant for DFT-MD simulations, a free energy functional  $F[n(\mathbf{r})]$  is used instead of  $E[n(\mathbf{r})]$ . These theorems have a huge advantage over the usual formulation of quantum mechanics, because they basically say that we do not need to solve the many-particle Schrödinger equation, we “only” need to find the electron density which yields the minimum energy. The difficult part is, how to find the “correct” energy functional  $E[n(\mathbf{r})]$  and how to calculate from this the ground state energy and density.

The basis of DFT is the energy functional  $E[n(\mathbf{r})]$ . While Hohenberg and Kohn and Kohn and Sham proposed functionals for constant and slowly varying density, the search for accurate functionals is still ongoing and the results of the calculations can depend heavily on the used functional [45]. Formally, the energy functional can be written in the form

$$E[n(\mathbf{r})] = V_{\text{ext}}[n(\mathbf{r})] + U_{\text{H}}[n(\mathbf{r})] + T_{\text{s}}[n(\mathbf{r})] + E_{\text{XC}}, \quad (1)$$

where

$$V_{\text{ext}} = \int v_{\text{ext}}(\mathbf{r})n(\mathbf{r})d^3r \quad (2)$$

is the energy due to the external potential  $v_{\text{ext}}(\mathbf{r})$ ,

$$U_{\text{H}}[n(\mathbf{r})] = \frac{1}{2} \int \int \frac{n(\mathbf{r})n(\mathbf{r}')}{|\mathbf{r} - \mathbf{r}'|} d^3r d^3r' \quad (3)$$

is the Hartree energy,

$$T_{\text{s}}[n(\mathbf{r})] = \sum_i^N \int \phi_i^*(\mathbf{r}) \left( -\frac{1}{2} \nabla^2 \right) \phi_i(\mathbf{r}) d^3r \quad (4)$$

is the Kohn-Sham kinetic energy, and  $E_{\text{XC}}$  is the so-called exchange-correlation (XC) functional. Note that Hartree atomic units are used throughout this chapter. In this XC functional all unknown properties of the interacting system are gathered, and this functional is the central ingredient for DFT calculations.

The simplest approximation is the local density approximation (LDA) [46–48] where the XC contribution is calculated for a homogeneous electron gas at the local density  $n(\mathbf{r})$ . This treatment is correct for slowly varying electron densities and yields the correct limiting case for very high densities. Generalized gradient approximations (GGA) are a better approach, where the XC functional depends not only on the electron density, but also on its gradient. The GGA by Perdew, Burke, and Ernzerhof (PBE) [49] is used for most results shown in Sect. 3, except for few calculations with the hybrid functional proposed by Heyd, Scuseria, and Ernzerhof (HSE) [50, 51]. Even better XC functionals are computationally much more demanding, and up to now not feasible for large-scale simulations.

Since the beginning of DFT in 1965 up till now more than 50 XC functionals have been developed, partly based on empirical data and partly based on ab initio theory. Several works are dedicated to benchmarking different functionals for e.g. lattice constants [45, 52–56], bulk moduli [52, 53], bond lengths [57–59], and band gaps [53, 54]. In general, there is no XC functional which performs equally well for all properties and all elements.

The PBE functional yields often not the most accurate results, but for many applications it performs quite well compared to its computational demands. Additionally, it is an ab initio functional in the sense that it is nonempirical. One of the main problems of the PBE functional (and other LDA and GGA functionals as well) is the self-interaction error, i.e. they are not self-interaction free, leading to too small band gaps [60, 61]. In principle, this can be improved by better functionals like HSE [53, 61] or EXX-LDA [62], however, with much higher computational costs.

The Hohenberg-Kohn theorems were used by [46] to derive a set of equations

$$\left( -\frac{1}{2} \nabla^2 + v_{\text{eff}}(\mathbf{r}) \right) \phi_i(\mathbf{r}) = \varepsilon_i \phi_i(\mathbf{r}), \quad (5)$$

$$n(\mathbf{r}) = \sum_i^N |\phi_i(\mathbf{r})|^2, \quad (6)$$



$$v_{\text{eff}} = v_{\text{ext}}(\mathbf{r}) + \int \frac{n(\mathbf{r}')}{|\mathbf{r} - \mathbf{r}'|} d^3 r' + \frac{\delta E_{xc}}{\delta n(\mathbf{r})}, \quad (7)$$

which have to be solved self-consistently, thus reformulating the many-body Schrödinger equation into a set of effective one-particle Schrödinger equations. Hereby, an iterative recipe to solve the problem is available, by starting from a guessed ground state density  $n(\mathbf{r})$ , constructing the effective potential  $v_{\text{eff}}$  (Eq. 7), solving Eq. 5, and calculating the new density  $n(\mathbf{r})$  (Eq. 6). This iteration has to be performed until the energy is converged, see also Fig. 4.

## 2.2 Numerics and Convergence

For the evaluation of the Kohn-Sham equations, one has to represent the wavefunctions in a convenient way. Many available codes use an expansion into plane waves, which have useful features for calculations, e.g. the implementation of periodic boundary conditions is straightforward and Fourier transformations can easily be done. One problem of plane waves is the representation of the wavefunctions near the ions, since the Coulomb potential leads to strong oscillations. To represent these oscillations many plane waves are needed, which make calculations very demanding. To circumvent this problem, pseudopotentials were introduced. The general idea is to replace the wavefunctions inside a sphere around the ions with smooth functions, without changing the physical outcome of the calculations. The first pseudopotentials introduced where the so-called norm-conserving pseudopotentials [63, 64], which conserved the norm of the wavefunctions at the sphere boundary. But still, for some elements, e.g. transition-metal elements or elements with  $d$  or  $f$  electrons, very “hard” pseudopotentials, i.e. small sphere cutoff radii, are needed, which still leads to high plane wave cutoffs. This could be solved by ultrasoft pseudopotentials [65] which relaxed the norm-conserving condition at the cost of a more involved pseudopotential generation. However, these generated pseudopotentials have to be tested extensively [66]. A better approach is the projector augmented wave (PAW) method [66, 67] which is based on a linear transformation between the all-electron and pseudo-wavefunctions. In principle, all these techniques are only of technical nature, i.e. they should only reduce the computational costs without changing the physical outcome. This has to be checked carefully in convergence tests with respect to plane wave cutoff (number of plane waves), and the radial augmentation cutoff.

Due to the periodic boundary conditions it is necessary to perform some of the calculations in reciprocal space by integrating over the Brillouin zone. However, for DFT-MD simulations it is not possible (and usually not needed) to sample the Brillouin zone with a very fine grid, so that the integration is replaced by a summation over some special  $\mathbf{k}$  points. In fact, often only one special  $\mathbf{k}$  point is needed, but obviously this calls for convergence tests with respect to the  $\mathbf{k}$ -point sampling. There are several possibilities to sample the Brillouin zone. One very

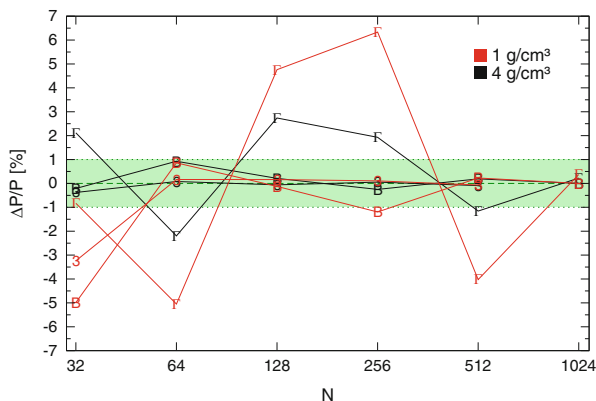


**Fig. 5** Convergence of the pressure with respect to the particle number for the  $\Gamma$  point ( $\Gamma$ ), the BMVP (B), and a  $3 \times 3 \times 3$  Monkhorst-Pack grid (3). Shown are results for liquid hydrogen at a density of  $1 \text{ g/cm}^3$  (red) and  $4 \text{ g/cm}^3$  (black) and a temperature of 1,000 K

common way for DFT-MD simulations is to use only the  $\Gamma$  point. Choosing this point has (apart from being only one point) the advantage that the wavefunctions have real values and the code does not need to deal with complex numbers, which can speed up the calculations. However, one has to check very carefully if the results are converged, which is sometimes only the case for higher particle numbers compared to other choices.

A common method for choosing more  $\mathbf{k}$  points is the method of Monkhorst and Pack [68] where a discrete grid of  $\mathbf{k}$  points is generated. Another special point that can be used instead is the so called “Baldereschi mean-value point” (BMVP) [69]. It has the advantage that many quantities converge very fast with respect to higher  $\mathbf{k}$ -point sets. An example for convergence tests with respect to  $\mathbf{k}$ -point sampling and particle number is shown in Fig. 5, where the good convergence of the BMVP for hydrogen simulations can be seen.

By using the Born-Oppenheimer approximation, one can perform classical MD simulations for the ions, and use DFT for the electrons. The basic principle is illustrated in Fig. 4. Like the classical MD simulations it starts with an ion configuration inside a simulation box. These ions provide the external potential for the DFT calculations for the electron system. With a (guessed) initial electron density  $n(r)$  the Kohn-Sham equations are solved, and from the Kohn-Sham eigenvalues and wavefunctions a new electron density and the resulting energy functional can be calculated. This procedure can be repeated with the new electron density, until the energy functional reaches its minimum. Afterwards the forces on the ions are calculated from the Hellmann-Feynman theorem [70] and, as in the classical MD simulations, the ions are moved in a finite timestep. In this way the forces are calculated ab initio for each timestep and the fundamental problem of

classical MD simulations (knowing the potential) can be solved. This workflow is implemented in several codes such as VASP [22, 37–39] and abinit [71, 72].

### 2.3 Electrical Conductivity

Within DFT the dynamic electrical conductivity can be calculated with the Kubo-Greenwood formula [73–78]

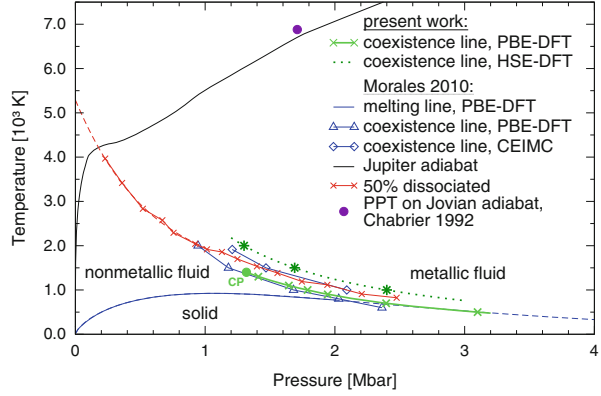
$$\sigma(\omega) = \frac{2\pi}{3V\omega} \sum_{\mathbf{k}} w_{\mathbf{k}} \sum_{j=1}^{N_b} \sum_{i=1}^{N_b} [f_{j,\mathbf{k}} - f_{i,\mathbf{k}}] \times |\langle \phi_{j,\mathbf{k}} | \hat{\mathbf{p}} | \phi_{i,\mathbf{k}} \rangle|^2 \delta(\varepsilon_{i,\mathbf{k}} - \varepsilon_{j,\mathbf{k}} - \omega), \quad (8)$$

where  $V$  is the volume of the simulation box and  $\omega$  the frequency. The summation over the matrix elements of the Kohn-Sham orbitals with the momentum operator  $\hat{\mathbf{p}}$ , weighted with the difference of the Fermi occupation numbers  $f_{i,\mathbf{k}}$ , is performed over all  $N_b$  bands. This is, however, very time consuming and needs much disk space. Therefore, it cannot be calculated for each timestep of the simulation, but only for snapshots of the simulation. Convergence tests have to be done with respect to the  $\mathbf{k}$ -point sum [79]. Additionally, it is possible within the Kubo theory to derive the thermal conductivity and the thermopower [78]. While it is possible to calculate optical properties like the reflectivity from the dynamic conductivity [78, 80], only results for the static limit ( $\omega \rightarrow 0$ ) are shown in Sect. 3.

Since the Kubo-Greenwood formula evaluates transitions between discrete energy eigenvalues obeying energy conservation via  $\delta(E_{i,\mathbf{k}} - E_{j,\mathbf{k}} - \omega)$ , the electrical conductivity is zero most of the time and has only finite values when the frequency  $\omega$  is equal to an exact energy difference between two bands. However, since the simulation can only be performed for a given number of electrons in a finite box, the bands form a discrete spectrum while they lie energetically very close for a real system. To circumvent this (unphysical) problem, the  $\delta$ -function is replaced by a Gaussian with a finite width. Depending on this width the dynamical conductivity will be more or less smooth.

But still, the conductivity would drop down for small  $\omega$ , approximately when  $\omega$  is smaller than the mean band distance. In general this effect can be reduced with higher particle numbers, since then the mean band distance gets smaller. Nevertheless, the direct limit of  $\omega = 0$  cannot be reached. Two approaches are possible for obtaining this limit. In the first approach, the width of the Gaussian can be increased, until smooth functions up to  $\omega = 0$  are obtained. But especially for small particle numbers the resulting static conductivity would depend very much on the chosen width and the results would be to some extent arbitrary. A better approach is to perform a regression (either a linear or an exponential function) in the area of small frequencies which are still higher than the mean band distance.

**Fig. 6** High pressure phase diagram of hydrogen. Present work (green) within PBE-DFT [87] and HSE-DFT (W. Lorenzen, unpublished) is compared with that of Morales et al. (blue) [86] using PBE-DFT and CEIMC. Also shown are their melting line (blue solid), the Jupiter adiabat (black line) [89], and a red line characterizing 50 % dissociation [90]



By this approach the unphysical drop in the conductivity due to the finite system size is ignored, but a reasonable limit can be obtained.

Note that this Kubo-Greenwood formalism applies only to the electronic contribution to the conductivity. In principle it is possible to calculate the ionic conductivity from DFT-MD simulations [81], but the effective charges carried by each ion have to be known, which is very involved for complex mixtures [82].

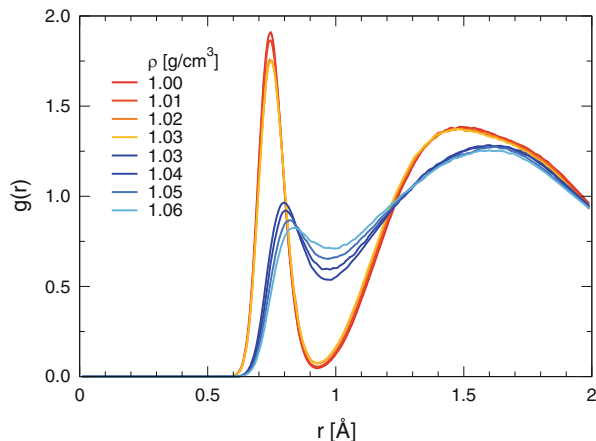
### 3 Ab Initio Results for WDM

#### 3.1 Hydrogen

Hydrogen as the simplest element is an ideal test case for WDM research. At the same time it is the most abundant element in the universe and the largest constituent of GPs. Especially for modeling GPs, the EOS for hydrogen is needed, which was therefore the aim of many studies, see e.g. [78, 83–85]. However, the main uncertainty and the main discrepancy between chemical models and the DFT-MD simulations was the existence of a first-order liquid-liquid phase transition from a nonmetallic molecular fluid to a dissociated metallic liquid (PPT). With the recent progress of ab initio simulations the existence of this phase transition seems to be clear [86, 87] and the problem is now reduced to determining the exact location of the transition. However, the experimental validation is still missing. An anomaly in the heating curve of liquid hydrogen was obtained recently [88] using pulsed lasers at static pressures in the Mbar region; this feature is closely correlated with our theoretical predictions for the PPT.

In Fig. 6 the high pressure phase diagram of hydrogen is shown. At temperatures below 1,000 K solid hydrogen occurs in various phases which are also of great interest, see [84, 85]. At higher temperatures, but still below 2,000 K, the above mentioned first-order phase transition is found. This liquid-liquid transition is

**Fig. 7** Proton-proton pair correlation functions  $g(r)$  at 700 K for densities near the phase transition [87]. The molecular peak vanishes abruptly at  $1.03 \text{ g/cm}^3$  indicating that the transition is driven by dissociation of  $\text{H}_2$  molecules



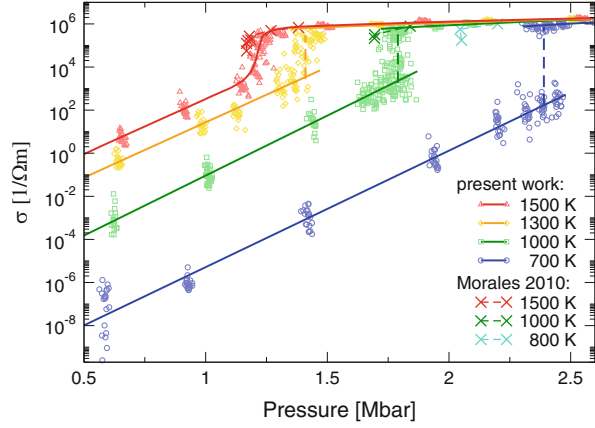
characterized by pressure dissociation as derived from the abrupt vanishing of the molecular peak, see Fig. 7. Simultaneously, a nonmetal-to-metal transition occurs which is reflected in the electrical conductivity data, see Fig. 8. The strong increase in the molecular phase (semiconducting fluid) is followed by a jump over 1–2 orders of magnitude when crossing the coexistence line. An almost temperature and density independent behavior is observed in the dense metallic fluid. The jump disappears above the critical point and the increase is steep but continuous there.

However, as can be seen from Fig. 6, the XC functional used in the DFT-MD simulations has an influence on the location of the liquid-liquid phase transition since the underlying nonmetal-to-metal transition is induced by bandgap closure. The PBE XC functional is known to yield too small bandgaps so that the transition pressure is underestimated (green line with crosses and blue line with triangles). More reliable results are expected using the HSE nonlocal XC functional (preliminary results are shown by the green dotted line with stars) and CEIMC simulations (blue line with diamonds). The impact of nuclear quantum effects and of van der Waals corrections in addition to that of a nonlocal XC functional as shown above has been studied recently [91].

### 3.2 Hydrogen-Helium Mixtures

A prominent example for a mixture in WDM is hydrogen and helium. This mixture is especially important for astrophysical objects, since hydrogen is in principle always accompanied by helium. Most of the modeling so far applies mixing rules to describe the properties of the mixture, especially for the EOS. However, more and more studies are devoted to the real mixture, see e.g. [92, 93]. An important effect which cannot be explained with mixing rules is the demixing of hydrogen and helium at high pressures. In particular, this process has been predicted to occur

**Fig. 8** Electrical conductivity for various isotherms [87]. The molecular phase is a semiconducting fluid. A jump occurs whenever crossing the coexistence line. An almost temperature and density independent slope is characteristic of the metallic fluid



in Saturn which would influence the thermal evolution of this planet strongly, see Sect. 4.3. To calculate this effect, one has to evaluate the Gibbs free energy of mixing

$$\Delta G(x) = \Delta U(x) + P\Delta V(x) - T\Delta S(x), \quad (9)$$

where  $G$  is the Gibbs free energy,  $U$  the internal energy,  $P$  the pressure,  $V$  the volume,  $T$  the temperature, and  $S$  the entropy. The  $\Delta$  denotes the difference between the mixed state and a linear mixing of the pure systems, e.g.  $\Delta U(x) = U(x) - xU(1) - (1-x)U(0)$ . Whenever the system can minimize its Gibbs free energy by demixing into two phases with different helium fractions  $x$ , demixing occurs. The only problem in DFT-MD calculations is the difficulty to access the entropy of mixing. The simplest approach is to use the ideal entropy of mixing

$$\Delta S_{\text{id}}(x) = -k_B [x \ln x + (1-x) \ln(1-x)], \quad (10)$$

while in principle better results can be obtained with thermodynamic integration techniques [94]. Two recent results for conditions in the interior of Jupiter and Saturn are shown in Fig. 9, in comparison to the phase diagrams of pure hydrogen and helium. The isentropes of both Jupiter and Saturn enter the demixing region at about 1 Mbar. While the jovian isentrope leaves the demixing region again at about 2.5 Mbar, and therefore has only a small fraction of its interior inside this region, the whole interior of Saturn is in the demixing region. This implies only a small effect on the structure and evolution of Jupiter, but has drastic effects on the evolution of Saturn, see Sect. 4.3. New results for lower pressures, i.e. in the molecular phase of hydrogen are in preparation [104]. All recent ab initio results reduced the uncertainty in the demixing temperatures drastically compared with previous predictions [13, 105, 106].

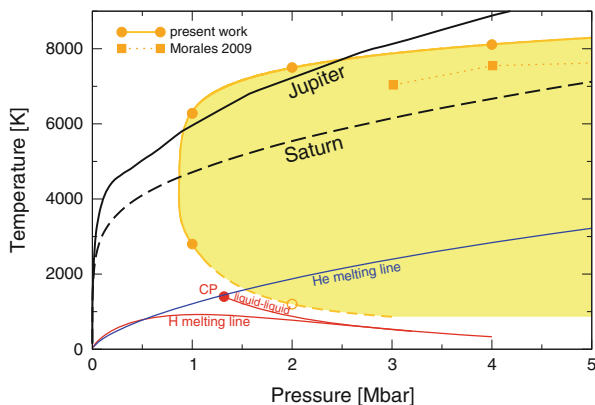


**Fig. 9** Demixing region (yellow area) for a helium fraction of  $x = 0.086$ , i.e. the mean helium fraction in the planetary interiors, in comparison with the isentropes of Jupiter [95] (solid black) and Saturn (dashed black), see [96]. The filled circles are the calculated data from the Gibbs free energy, the open circle at 2 Mbar is extracted from conductivity data. The line is a fit to these points. The results of Morales et al. [94] for the demixing line are also shown (squares). We compare with the phase diagram of pure hydrogen (red). The melting line is taken from Ref. [86] and the coexistence line of the liquid-liquid phase transition with its critical point from Ref. [87]. For helium we show the melting line (blue; Kechin-type fit [97] to experimental data [98–102]) and our recent high-pressure prediction [103]

### 3.3 Equation of State and Shock Wave Experiments for Hydrogen

Probing the EOS in the WDM regime is a challenging task. Sophisticated experiments have to be performed to reach such extreme conditions. Pressures of several megabar can be generated using static diamond anvil cells or dynamic compression methods. Drivers for strong shock waves are, e.g., high-power lasers [107, 108], gas guns [109, 110], pulsed power [111, 112], or chemical explosions [113, 114]. For instance, all final states of single shock experiments performed with deuterium are located on the principal Hugoniot curve for a given initial state in the cryogenic liquid at 20 K and 0.17 g/cm<sup>3</sup>. Recent experiments indicate a maximum compression of about 4.25–4.5 [108, 111, 115, 116]. States off the principal Hugoniot can be reached by varying the initial condition, e.g. by using a precompressed sample [117], by applying reverberation techniques [109, 111, 116], or by generating quasi-isentropic compression paths [118, 119]. All techniques but the last one yield the thermal EOS  $P(\rho, T)$  or at least  $P(\rho)$ . Up to now, quasi-isentropic experiments only measure the compression ratio and determine pressures and temperatures via an EOS that is used in a hydrocode in order to reproduce the same compression.

Ab initio EOS data are benchmarked by shock wave experiments measuring  $P(\rho, T)$  or  $P(\rho)$ . In Fig. 10 experimental data for the principal Hugoniot (orange

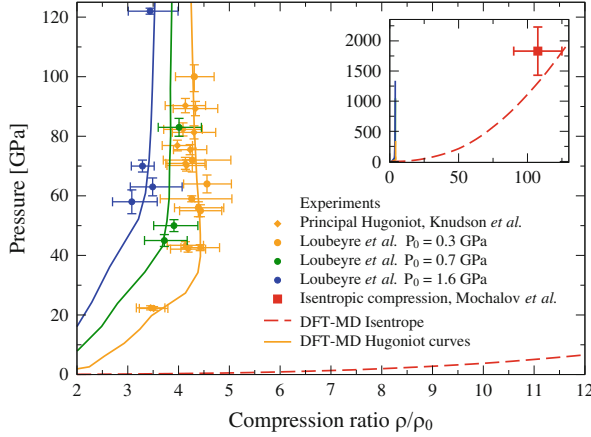


**Fig. 10** Isentropic compression of deuterium (red dashed) starting at  $0.04 \text{ g/cm}^3$  and  $283 \text{ K}$  reaches 108-fold initial density (inset) [119]. Hugoniot experiments with precompressed targets (circles) [117] start at  $300 \text{ K}$  and  $0.087 \text{ g/cm}^3$  (orange),  $0.12 \text{ g/cm}^3$  (green) and  $0.16 \text{ g/cm}^3$  (blue). The orange curve is almost identical with the principal Hugoniot starting at  $20 \text{ K}$  and  $0.0855 \text{ g/cm}^3$  for which we show data (diamonds) [111]. Solid and broken lines are DFT-MD results [120]

circles [117] and diamonds [111]) and Hugoniot curves for precompressed states of deuterium (blue and green circles [117]) are shown as well as a point representing a 108-fold compression of gaseous deuterium [119]. The DFT-MD Hugoniot curves for different initial conditions fixed by the experiment are derived from our ab initio EOS data [120] which coincide with another ab initio data set [84]. Both reproduce the experimental pressures very well while they underestimate the temperature onset of dissociation slightly [117]. This is again due to the bandgap problem when using the GGA-PBE functional. Note that higher precompression leads to smaller compression ratios. This has been shown earlier for hydrogen [84, 121] and helium [122].

Quasi-isentropic compression paths can be reconstructed evaluating Eq. (12) in Sect. 4.1 with a given EOS. We calculate the compression paths of deuterium starting from an initial temperature of  $283 \text{ K}$  and a density of  $0.04 \text{ g/cm}^3$  [119] using our DFT-MD data [120]. For the measured compression ratio we expect a final pressure of  $\sim 13 \text{ Mbar}$  at  $1,500 \text{ K}$ , significantly lower than the predicted  $18 \text{ Mbar}$  at  $3,500 \text{ K}$  as derived from a semi-empirical EOS used in the hydrocode. However, the data point is located on a quasi-isentrope, see Fig. 10, illustrating impressively that high pressures and low temperatures as relevant for states deep in planetary interiors can be reached in the laboratory today. More accurate experiments should be performed to discriminate between competing interior models and, thus, competing EOS data; see next Sect. 3.4.



### 3.4 Water

After hydrogen and helium, carbon, nitrogen and oxygen (and neon) are the next abundant elements. Thus, the high-pressure behavior of their hydrides  $\text{CH}_4$ ,  $\text{NH}_3$  and  $\text{H}_2\text{O}$ , and that of their mixtures, is of great interest in planetary physics, especially for Uranus and Neptune in the solar system [123]. This is further highlighted by the fact that Neptune-like exoplanets might be very common, see Fig. 3. We review here some new results for *warm dense water* as a prototypical example for molecular systems. A better knowledge of their high-pressure behavior is a prerequisite for an advanced understanding of the structure and evolution of such exoplanets.

Extensive DFT-MD simulations were performed to determine the EOS and the transport properties of warm dense water [21, 81, 124, 125]. We show in Fig. 11 the high-pressure phase diagram as predicted in Ref. [17]. Increasing the temperature in the liquid phase transforms water continuously from a molecular through a dissociated (ionic) to a plasma region (with *free* electrons). At high pressures we find various solid (ice) phases and, most interestingly, also an exotic superionic phase as predicted earlier [21, 124]. This phase consists of an oxygen lattice but mobile protons which would represent a proton conductor. The type the oxygen lattice under these conditions is still under debate, whether or not it retains the bcc structure of the high-pressure ice VII and ice X phases, or transforms to a fcc lattice with a slightly higher melting line [19].

The total electrical conductivity of warm dense water is shown in Fig. 12. The electronic contribution is calculated via the Kubo-Greenwood formula (8) using the HSE XC functional in order to obtain correct bandgaps [81]. The ionic contribution is determined by assigning an effective charge to the protons, see [21]. This analysis based on the diffusion coefficients can be improved by applying, e.g., polarization theory within each MD timestep in order to determine the effective charge of the proton rigorously which is, however, numerically very demanding [82]. It turns out that both methods agree well for warm dense water but not for the superionic phase where cross correlation terms (which are neglected in the diffusion analysis) have to be considered.

The curves show a systematic increase of the total conductivity with density and temperature. In the fluid phase below 4,000 K, the conductivity is mostly due to protons while the electronic contribution dominates at higher temperatures. Interestingly, the conductivity drops slightly (factor two) along the plasma-to-superionic phase transition (dotted lines). This is due to an increased localization of the electrons which stabilizes the oxygen lattice. At higher densities the conductivity increases again so that a nonmetal-to-metal transition is predicted in the superionic phase, simultaneously with a proton rearrangement. Protons occupy ice X sites more frequently at lower densities but favor octahedral sites in the high-density regime.

Shock-wave experiments with a so far unprecedented accuracy were performed recently at the Sandia Z machine that allow us to benchmark the high-pressure water EOS. We show the corresponding Hugoniot data for water (red symbols)

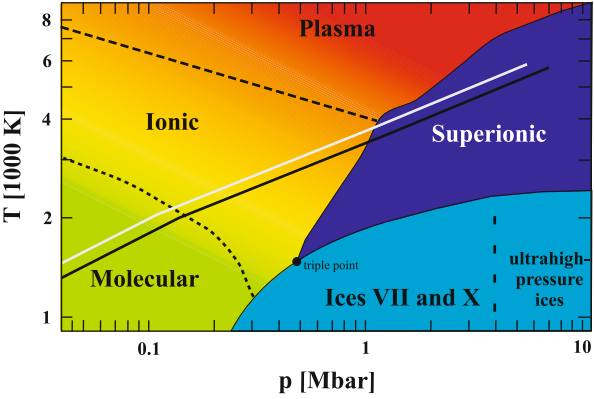


**Fig. 11** High-pressure phase diagram of water [17]. The liquid phase includes a molecular, a dissociated (ionic) and a plasma region at higher temperatures. Besides the various solid phases (shown are ice VII and ice X), an exotic superionic phase is predicted. see also [19, 21, 124]. For comparison the theoretical isentropes of the water-rich planets Uranus (*grey solid*) and Neptune (*black solid*) are shown as well

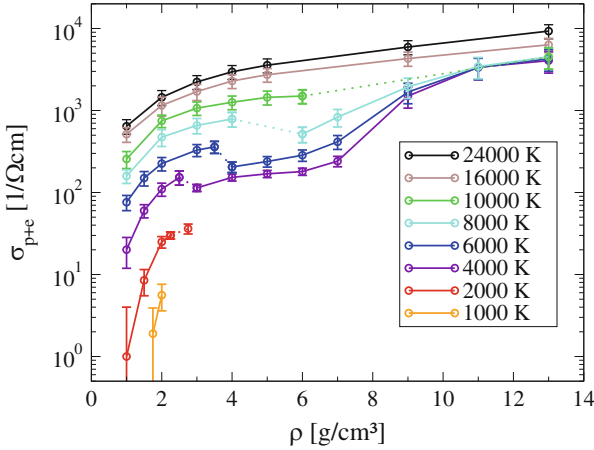
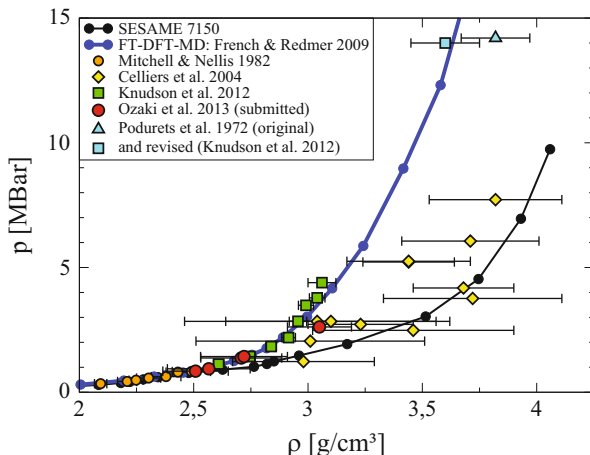


**Fig. 12** Total electrical conductivity of water, i.e. electron plus proton contribution [81]. The *dotted lines* indicate the location of the phase transition between the plasma and the superionic phase, see Fig. 11

in Fig. 13 [126]. The  $Z$  data are in good agreement with gas gun data [128] and explosively driven shock data [129] but indicate a significantly lower compressibility than laser-driven shock data [130]. The vastly reduced uncertainty in the new  $Z$  data (roughly an order of magnitude), strongly suggests that water is much less compressible than the standard Sesame model predicts, and that water is instead very accurately described by ab initio EOS data [125, 131]. Furthermore, the reanalyzed ultra-high pressure point [132] is also in very good agreement with the ab initio

**Fig. 13** Hugoniot curve for water. Z data (green boxes [126]) are compared with laser data (yellow diamonds [130] and red circles [127]) and gas gun data (orange circles [128]). Models include SESAME (black line) and DFT-MD (blue line [131]). The high-pressure point of Podurets et al. (light blue triangle [132]) has been reanalyzed (light blue box)



EOS. Thus, with the exception of the laser data, the EOS based on DFT-MD for water matches all experimental Hugoniot data up to 1.4 TPa. Furthermore, very good agreement is also achieved for second shock data and the reflectivity along the principal Hugoniot curve, see [126] for details. We conclude that this ab initio EOS can now be used to construct more reliable interior models for Uranus and Neptune [8, 17, 133], see also Sect. 4.2 and Fig. 17, but also for water-rich exoplanets, e.g., for GJ 436b [31] and the Super-Earths and Sub-Neptunes in the Kepler 11 system [18].

Similar experimental and theoretical studies are performed for ammonia [124, 134–141] and methane [134, 142–144] which have a rich phase diagram as well. Of central importance in this context is the treatment of multi-component C-N-O-H-He mixtures. Corresponding EOS data would serve as a new and more realistic data base for interior, evolution, and dynamo models of Neptune-like planets. These studies are closely connected with *high-pressure chemistry* since chemical equilibria are shifted at extreme conditions and new reaction channels might occur which are not important at ambient conditions. Interesting effects such as demixing and polymerization might occur as well. First promising results were obtained for a *synthetic* Uranus composition of H:O:C:N = 28:7:4:1 [145] and mixtures of CH<sub>4</sub> and H<sub>2</sub>O [146].

### 3.5 Other Materials

The detection of Super-Earths has enhanced the interest in geophysics and initiated studies of the high-pressure behavior of typical mantle materials like MgO, SiO<sub>2</sub>, MgSiO<sub>3</sub>, CaSiO<sub>3</sub> etc. on a large scale; for reviews, see [147–150]. For instance, new predictions for the melting line based on ab initio simulations [151, 152]

and a first-order liquid-liquid phase transition in silicate melts derived from laser-driven shock compression experiments were given [153] which could be important for stabilizing convective layering and compositional stratification in Super-Earths. These data are needed to predict, e.g., accurate mass-radius relationships for exoplanets [154] and the interior structure of Super-Earths [155].

Furthermore, extended data sets are generated for warm dense Fe, Ni, and Fe-Ni alloys which are expected to be the dominant core materials of rocky, ice-giant and gas-giant planets, including exoplanets. Of central importance in this context is the phase diagram of iron. Various phases transformations are predicted in the solid up to 1 Gbar (bcc-hcp-fcc-bcc) [156]. The slope of the high-pressure melting line is important for deciding whether or not the inner core of Super-Earths is solid (as in the Earth) or liquid [157, 158]. Solidification of iron at the boundary between the inner (solid) and outer (liquid) core is critical for the planetary magnetic field because most of the lighter elements are excluded from the inner core upon freezing into the corresponding lattice structure which releases most of the energy that drives convection and, thus, the planetary dynamo. The strength of the planetary magnetic field also depends on the electrical conductivity of solid and liquid iron under such conditions [159]. The influence of lighter elements on the electrical conductivity of, e.g., liquid Fe-Si and Fe-O alloys is also crucial [160]. For instance, the slope of the high-pressure melting line of iron decides whether or not Super-Earths are just up-scaled Earths (with an outer liquid core above an inner solid core) or solid bodies [161–163]. This is of paramount importance for the generation of possible magnetic fields and, thus, for the existence of even simplest life-forms on exoplanets.

## 4 WDM and Giant Planets

In this section we outline how giant planets serve as astrophysical laboratories for WDM calculations since typical parameters for their deep interior cover pressures of several ten Mbar and moderate temperatures of few eV, see Sect. 1. In particular, we discuss the influence of the plasma phase transition (PPT) in hydrogen (Sect. 3.1) and of demixing in hydrogen-helium systems (Sect. 3.2) on the interior and evolution of GPs, especially of Jupiter and Saturn.

### 4.1 Interior Models for Jupiter and Saturn

Interior structure models for Jupiter and Saturn have been calculated for decades, see e.g. [7, 89, 95, 164–169]. Those models have to reproduce all observational constraints, see Sect. 1.2, especially the shape of the gravity field. Caused by the rather rapid rotation of the planet (for Jupiter and Saturn, the rotational period is  $\sim 10$  h, for Uranus and Neptune  $\sim 17$  h) its gravitational field departs from a purely

spherical function. To describe these deviations the field is expanded into Legendre polynomials  $P_{2i}(\cos \Theta)$  with the polar angle  $\Theta$ ,

$$V(r, \Theta) = -\frac{GM}{r} \left( 1 - \sum_{i=1}^{\infty} \left( \frac{R_{eq}}{r} \right)^{2i} J_{2i} P_{2i}(\cos \Theta) \right), \quad (11)$$

with the gravitational constant  $G$  and the equatorial radius  $R_{eq}$ . The gravitational moments  $J_{2i}$  can be measured through the analysis of the orbits of planetary satellites and of the trajectories of spacecraft flybys. These *constraints* have to be matched by any theoretical interior model that uses EOS data for the relevant planetary materials at WDM conditions. This is realized in the standard three-layer model by redistributing the amount of heavy elements within both adiabatic layers, see [170]. For a corresponding multi-layer approach including double-diffusive convection and compositional gradients, see [171].

A central goal of these efforts is the determination of the size of the planetary cores which would give valuable information on the formation process of planets, i.e. either via core accretion [172, 173] or via disk instability [174, 175]. Even for Jupiter, the prototypical and best studied GP in the solar system, the predictions vary from light cores ( $8.3 M_E$  [165],  $5 M_E$  [166],  $(3-3.5) M_E$  [167],  $(0-14) M_E$  [168],  $(0-8) M_E$  [89]) to massive ones  $(14-18) M_E$  [169], see Fig. 14. Obviously there is still a big uncertainty whether Jupiter has a core or not. In contrast Saturn's core mass can be as high as  $20 M_E$  [176, 177].

While interior models based on the EOS for hydrogen and helium within a chemical picture proposed by Saumon, Chabrier, and van Horn [178] (SCvH-EOS) agree in predicting a rather small core for Jupiter, the first Jupiter models that used an ab initio EOS differed significantly in their core mass prognosis, as can be seen in Fig. 14. The underlying planetary models are a three-layer model in case of Nettelmann et al. [89], using LM-REOS and fitting the gravity data by choosing corresponding metallicities in the two envelopes, and a two-layer model in the approach of Militzer et al. [169] who also use a DFT-MD based EOS and assume deep zonal winds to fit  $J_4$ . This discrepancy was resolved recently by Militzer [182] who showed that linear mixing of separate ab initio EOS for hydrogen and helium, as performed by Nettelmann et al., leads to the same results for an adiabat under Jovian conditions as derived from a real mixture of hydrogen and helium via thermodynamic integration.

A three-layer interior model (see Fig. 1) of Jupiter that fulfills all observational constraints is shown in Fig. 15. The model shown here has a transition pressure of 8 Mbar between the two adiabatic layers at 0.629 of Jupiter's radius, a core of  $3.56 M_E$ , a metallicity of 0.038 ( $\sim 2.5 Z_{\text{solar}}$ ) in the outer layer, and of 0.128 in the inner layer. The core-mantle boundary is characterized by a pressure of 42 Mbar at moderate temperatures of 19,500 K. Former models based on the SCvH-EOS [166] argue that the interior of Jupiter is influenced by the PPT in hydrogen with a critical point at  $T_c = 15,300$  K,  $P_c = 0.614$  Mbar and  $\rho_c = 0.35 \text{ g/cm}^3$  leading to a jump in entropy at 1.17 Mbar and 6,880 K. Their prediction for the critical point was shown

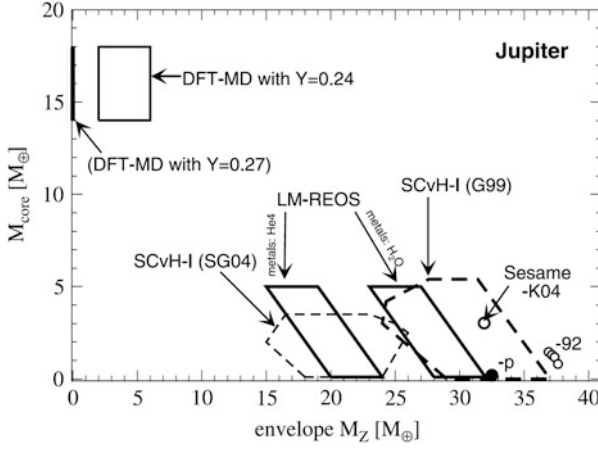


**Fig. 14** Core mass vs. metallicity for Jupiter using different EOS data and interior models [170]. Shown are results using the H- and He-Sesame-92 EOS [179] and a modified version of Kerley (K04) [180]. LM-REOS results use a scaled He-EOS (left quad) and the H<sub>2</sub>O-REOS (right quad) as a representative for metals. The other DFT-MD EOS [169] assumes  $Y_1 = Y$  throughout the envelope. The SCvH-I models taken from [181] (SG04) assume  $Z_1 = Z_2$  and those from [168] (G99)  $Z_1 \neq Z_2$

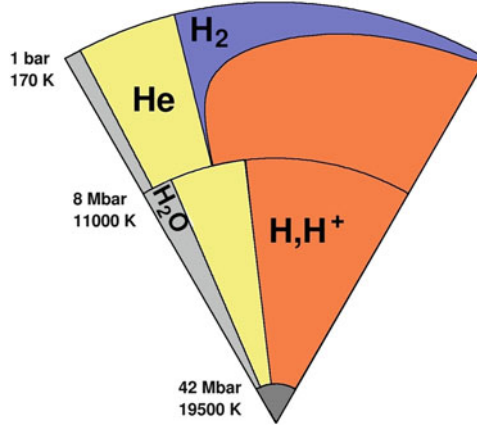
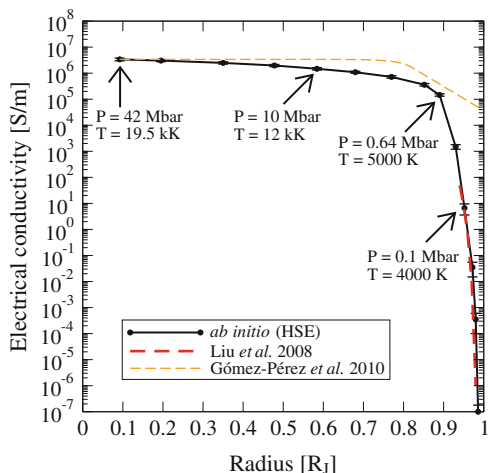


**Fig. 15** Jupiter model based on LM-REOS and a three-layer structure with a transition pressure  $P_{12} = 8$  Mbar at 0.629 of the Jovian radius [89, 186]. At the core-mantle boundary we find a temperature of 19,500 K and a pressure of 42 Mbar. The mass of the core amounts in this model  $3.56 M_E$ . The fraction of metals in the fluid layers is  $Z_1 = 0.038$  and  $Z_2 = 0.128$

in Fig. 6 (phase diagram of hydrogen) together with the Jovian isentrope according to Fig. 15. The isentrope, however, is not influenced by the PPT as we conclude from the available ab initio calculations, but by the continuous transition from the molecular to the conducting fluid which still occurs above the critical point. The red line taken from Tamblyn and Bonev [90] indicates 50 % dissociation in hydrogen

**Fig. 16** Electrical conductivity along the Jovian adiabat, see [186]. The *solid line* represents an evaluation of the Kubo-Greenwood formula 8 based on ab initio simulations using the HSE functional. It is in perfect agreement with the semiconductor model of Liu et al. [183] (*red dashed line*) based on experimental data. Also shown is a model of Gomez-Perez et al. [187] used in dynamo simulations of Jupiter's magnetic field



for a given P-T value. It intersects the isentrope just in the region where it flattens. The isentrope obeys the relation

$$\left(\frac{\partial T}{\partial \rho}\right)_S = \frac{T}{\rho^2} \left(\frac{\partial P}{\partial T}\right)_\rho = \frac{T}{\rho} \gamma \quad (12)$$

with the Grüneisen parameter  $\gamma$ . The change of temperature  $T$  with density  $\rho$  at constant entropy  $S$  is governed by the absolute values of  $T$  and  $\rho$  and the derivatives of the pressure  $P$  and the specific internal energy  $u = U/m$  with respect to  $T$  at constant  $\rho$ . The flattening of the isentrope is driven by the additional energy required to break the hydrogen bonds leading to an increasing denominator, namely  $c_v$ . This dissociation is accompanied by a sharp rise in electrical conductivity, see Fig. 16. It is calculated applying the Kubo-Greenwood formula (8) on VASP simulations using the HSE functional, see Sects. 2.3 and 3.1. The results are in very good agreement with a semiconductor model of Liu et al. [183] for the conductivity in the outer regions of Jupiter. It fits a linear decrease of the band gap with density according to shock wave data [109, 184, 185]. The conductivity and further material properties along the Jovian adiabat were calculated by French et al. [186]. These data will serve as a more realistic input in future dynamo simulations for planetary magnetic fields [187] that so far assume a superexponential behavior of the electrical conductivity (orange line in Fig. 16).

## 4.2 Interior Models for Uranus and Neptune

Jupiter and Saturn, which are mainly composed of hydrogen and helium have a mean density of  $1.33 \text{ g/cm}^3$  and  $0.69 \text{ g/cm}^3$ , respectively. However, Uranus and

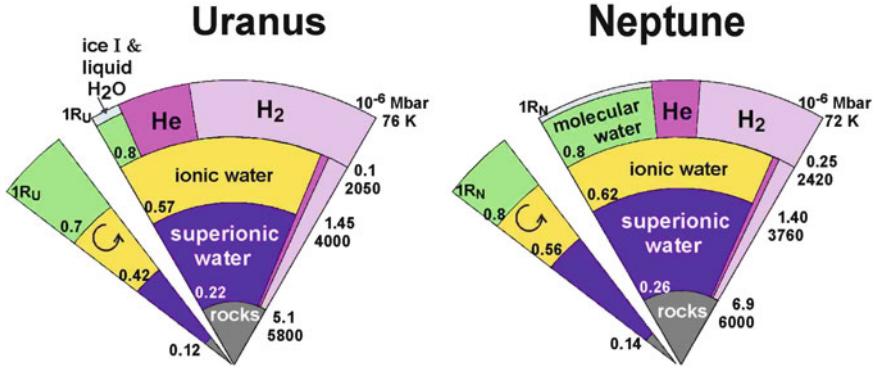


**Fig. 17** Three-layer interior models of Uranus and Neptune (a rocky core is surrounded by two adiabatic fluid H-He-H<sub>2</sub>O envelopes, larger pie charts on the *right*) [17] compared with predictions from magnetic field simulations (smaller pie charts on the *left*) [189, 190]

Neptune whose radii are only  $\sim 35\%$  of the Jovian one have mean densities of  $1.27 \text{ g/cm}^3$  and  $1.64 \text{ g/cm}^3$ , which implies that they must contain a larger fraction of heavy elements (metals) than Jupiter and Saturn. State-of-the-art interior models usually assume a rocky core surrounded by two adiabatic fluid envelopes composed of hydrogen, helium and water [8, 133, 188]. Water serves as representative for metals or, more specifically, represents the real C-N-O-H mixture inside these planets. This underlines the great need for accurate EOS and conductivity data for this prototypical molecular system or molecular mixtures at WDM conditions, see Sect. 3.4.

Interestingly, predictions for the interior of Uranus and Neptune were derived from three-dimensional magnetic field simulations [189, 190]. Their non-dipolar and non-axisymmetric magnetic fields are perhaps generated in a fairly thin layer of at most 0.3 planetary radii surrounding a conducting core that is fluid but stably stratified. In Fig. 17, these results (small pie charts) are compared with three-layer interior models described above [8, 17]. Numbers given on the left are the radius coordinates, numbers on the right denote pressure and temperature values. Below an envelope of helium and molecular hydrogen, water is the main constituent in its ionic phase (yellow) and, for more extreme conditions, in its superionic phase, see Fig. 11. A remarkable agreement of the interior composition of both planets which stem from two different modeling strategies (based solely on gravity data or the shape of the magnetic field) can be stated. However, the conditions for the occurrence of stably stratified layers in the deep interior have to be checked in more detail, e.g. by considering further properties of the superionic phase and possible demixing processes. A detailed analysis of the interior structure of both planets based on new gravity data is performed in Ref. [133].



### 4.3 Evolution of Giant Planets

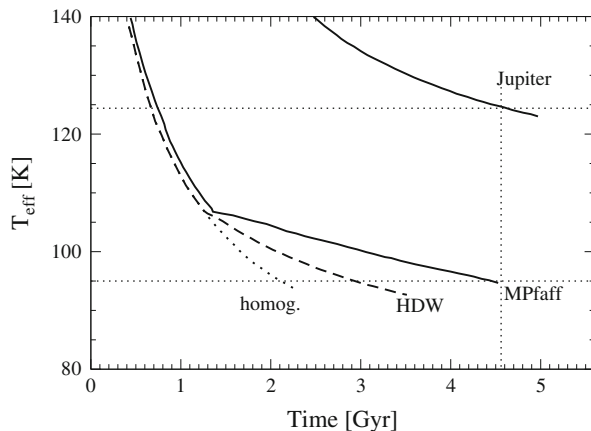
After formation in the disk around a young star, the initially warm, luminous and extended planets cool down and contract in a radiative quasi-equilibrium determined by the received radiation flux from the parent star and the emitted radiation of the planet. The received radiation, with a maximum in the visible range, is characterized by the equilibrium temperature  $T_{\text{eq}}$ , the temperature a black body would have solely exposed to the flux of the star, without internal sources. However, Jupiter and Saturn are observed to emit almost twice the energy they receive from the sun, suggesting intrinsic sources of energy. These sources are addressed via the effective temperature  $T_{\text{eff}}$ , the temperature of a hypothetical black body emitting the same total radiation as the observed planet does. The evolution of the planet, which is in principal the change of  $T_{\text{eff}}$  with time, can then be calculated using the cooling equation:

$$4\pi R_p^2 (T_{\text{eff}}^4 - T_{\text{eq}}^4) = - \int_0^M dm \frac{T(m, t) ds(m, t)}{dt}. \quad (13)$$

The left-hand side maps the intrinsic radiation source of the planet with radius  $R_p$ , since  $T_{\text{eq}}$  accounts for the influence of the pure solar radiation and  $T_{\text{eff}}$  that of the reflected solar radiation and the intrinsic planetary radiation sources. Knowing  $T_{\text{eq}}$  the evolution of  $T_{\text{eff}}$  is determined by the evolution of the total planetary heat content, given on the right-hand side of the cooling equation. The second law of thermodynamics relates the heat content to the entropy  $s = S/m$ , which is determined for the planet by  $T_{\text{eff}}$ , since the layers are isentropic. Integration of the heat content  $T(m, t) ds(m, t)$  of each mass shell over the whole planet leads to the total heat content. Its change with time yields the change of  $T_{\text{eff}}$  with time and hence the evolution of the planet by integrating the cooling equation backward in time, starting from a present model. The age of the solar system and thus the age of the planets is 4.56 billion years (Gyr). Accurate planetary models should reproduce this age for solar system planets in the associated evolution calculations.

If the amount of helium  $Y_n$  and heavy elements  $Z_n$  as well as the mass  $M_n$  of each mass shell (with index  $n$ ) are assumed to remain constant during time, the evolution is called homogeneous. On the contrary, a change of the particle concentration with time, see [191], leading to a change in  $Y_n$  or  $Z_n$ , or an extended inhomogeneous region in the planet, see [192], lead to an inhomogeneous evolution of a planet. The homogeneous evolution within one-layer models for Jupiter was first calculated by Hubbard predicting an age of 4–8 Gyr [193] and 5.1 Gyr [193]. Further calculations using the SCvH-EOS [178] with different model assumptions (see references) yield results of 5.2–5.3 Gyr [194], 4.2–5.2 Gyr [195], 4.7 Gyr [196], and 4.66 Gyr [89]. An example cooling curve for Jupiter is shown in Fig. 18. Obviously, homogeneous evolution models are suited to reproduce the correct age of Jupiter, which is also true for Neptune, predicting an age of 4.3–4.8 Gyr [133]. However, similar homogeneous evolution models for Saturn lead to an age of only 2–3 Gyr [194–198], suggesting

**Fig. 18** Homogeneous evolution for Jupiter (*solid*) and Saturn (*dotted*) and inhomogeneous evolution for Saturn with respect to the H-He demixing calculations of Hubbard and DeWitt [202] (*dashed*) and Pfaffenzeller et al. [106] (*solid*) taken from [203]



an additional internal energy source, and of 6.8–10 Gyr [133, 198] in case of Uranus, indicating a retarding effect of ineffective cooling.

The issue of Saturn’s short cooling time is closely related to the process of phase separation of hydrogen and helium at high pressures, see Sect. 3.2. First extensive studies on the “helium rain” in Saturn have been performed by Stevenson and Salpeter [191]. In the demixing region, helium is assumed to form droplets with a higher density than their surrounding so that they sink into deeper layers of the planet, thereby releasing gravitational energy and increasing the intrinsic luminosity. There is observational evidence that this process has been occurring in Saturn already for a long time (see Fig. 18) and that it has started in Jupiter as well. For instance, the protosolar He/H-ratio amounts 0.086. In case of Jupiter the Galileo entry probe measured a lower ratio of 0.079 [199], and infrared spectra measurements of Saturn’s atmosphere indicate a ratio between 0.055 and 0.08 [200]. In addition, the theoretical isentrope of Saturn above 1 Mbar proceeds well through the theoretical demixing region predicted by Lorenzen et al. [103] and by Morales et al. [94], see Fig. 9. The intersection of the Jovian isentrope with the demixing region indicates that demixing might occur in Jupiter as well. Alternatively, Leconte and Chabrier [201] demonstrated that multi-layer models for Saturn containing compositional gradients and double diffusive convection lead to a considerably slower cooling of the planet.

For illustration, we show here previous results of Fortney and Hubbard [196] in Fig. 18. Homogeneous evolution yields an age of only  $\sim 2$  Gyr (dotted line). An inhomogeneous evolution using the demixing calculations of Hubbard and DeWitt [202] would lead to an age of  $\sim 3$  Gyr (dashed line). Assuming that H-He separation is the most important additional intrinsic heat source, they modified the phase diagram of Pfaffenzeller et al. [106] in order to reproduce the correct age of Saturn (solid line). These calculations have been extended to extrasolar giant planets [203], where demixing should occur as well. Evolution calculations for Saturn based on the ab initio H-He EOS of Lorenzen et al. [103] are in progress.

## 5 Conclusions

In this chapter we have outlined the method of ab initio simulations that is perfectly suited to determine the thermophysical properties of WDM. Various fundamental problems such as the shape of the high-pressure phase diagram (i.e. location of the melting line and of solid-solid transitions, existence of a first-order liquid-liquid phase transition in hydrogen or of a superionic phase in water or ammonia), the consequences of a pressure-driven nonmetal-to-metal transition in molecular systems, and the demixing of hydrogen and helium can be addressed consistently. The corresponding EOS and conductivity data are essential for the development of advanced interior and dynamo models for solar and extrasolar GPs. The ab initio data can be benchmarked by state-of-the-art shock wave and x-ray Thomson scattering experiments, and excellent agreement is usually achieved. Furthermore, new observations for solar (e.g. via the Juno mission to Jupiter) and extrasolar GPs (e.g. via the Kepler and other planned space missions) will substantially extend our so far limited and perhaps not representative data base for planetary physics. We conclude that a better understanding of WDM is a key element for the future development of planetary physics which is fortunately accompanied by the rapid and coincidental progress in ab initio simulations and shock wave experimental technique.

**Acknowledgements** We thank Mandy Bethkenhagen, Daniel Cebulla, David Ceperley, Michael Desjarlais, Martin French, Sebastien Hamel, Bastian Holst, Jonathan Fortney, Nadine Nettelmann, Robert Püstow, and David Stevenson for many helpful discussions. This work was supported by the Deutsche Forschungsgemeinschaft within the SFB 652, SPP 1385, SPP 1488, and the grant RE 882/11. Support by the North-German Supercomputing Alliance (HLRN) and the ITMZ of the University of Rostock is greatly acknowledged. Pictures of solar planets are taken from NASA/JPL/University of Arizona. This research has made use of the Exoplanet Orbit Database and the Exoplanet Data Explorer at [exoplanets.org](http://exoplanets.org). We thank the Institute of Pure and Applied Mathematics, UCLA for the organization of the workshop series, the kind hospitality, and the support.

## References

1. V. Fortov, I. Iakubov, *Physics of Nonideal Plasma* (Hemisphere Publishing, New York, 1990)
2. Committee on High Energy Density Plasma Physics, National Research Council, *Frontiers in High Energy Density Physics: The X-Games of Contemporary Science* (The National Academies Press, Washington, DC, 2003)
3. R.W. Lee, S.J. Moon, H.K. Chung, W. Rozmus, H.A. Baldis, G. Gregori, R.C. Cauble, O.L. Landen, J.S. Wark, A. Ng, S.J. Rose, *J. Opt. Soc. Am. B* **20**(4), 770 (2003)
4. S.H. Glenzer, R. Redmer, *Rev. Mod. Phys.* **81**, 1625 (2009)
5. B. Remington, R. Cavallo, M. Edwards, D.M. Ho, B. Lasinski, K. Lorenz, H. Lorenzana, J. McNaney, S. Pollaine, R. Smith, *Astrophys. Space Sci.* **298**, 235 (2005)
6. R.P. Drake, *Phys. Plasmas* **16**(5), 055501 (2009)
7. T. Guillot, *Science* **286**, 72 (1999)
8. J.J. Fortney, N. Nettelmann, *Space Sci. Rev.* **152**, 423 (2010)

9. S. Udry, N.C. Santos, *Ann. Rev. Astron. Astrophys.* **45**, 397 (2007)
10. J.J. Fortney, S.H. Glenzer, M. Koenig, B. Militzer, D. Saumon, D. Valencia, *Phys. Plasmas* **16**(4), 041003 (2009)
11. I. Baraffe, G. Chabrier, T. Barman, *Rep. Progr. Phys.* **73**, 016901 (2010)
12. N. Haghighipour, *Contemporary Phys.* **52**(5), 403 (2011)
13. D.J. Stevenson, *Phys. Rev. B* **12**(10), 3999 (1975)
14. D.J. Stevenson, *Annu. Rev. Earth Planet. Sci.* **10**, 257 (1982)
15. P.P. Edwards, M.T.J. Lodge, F. Hensel, R. Redmer, *Phil. Trans. R. Soc. A* **368**, 941 (2010)
16. R. Redmer, B. Holst, in *Metal-to-Nonmetal Transitions. Springer Series in Material Sciences*, vol. 132, ed. by R. Redmer, B. Holst, F. Hensel (Springer, Berlin, 2010), pp. 63–84
17. R. Redmer, T.R. Mattsson, N. Nettelmann, M. French, *Icarus* **211**, 798 (2011)
18. E.D. Lopez, J.J. Fortney, N. Miller, *Astrophys. J.* **761**, 59 (2013)
19. H.F. Wilson, M.L. Wong, B. Militzer, *Phys. Rev. Lett.* **110**, 151102 (2013)
20. D.M. Ceperley, E. Manousakis, *J. Chem. Phys.* **115**, 10111 (2001)
21. A.E. Mattsson, P.A. Schultz, M.P. Desjarlais, T.R. Mattsson, K. Leung, *Model. Simul. Mater. Sci. Eng.* **13**, R1 (2005)
22. J. Hafner, *J. Comput. Chem.* **29**, 2044 (2008)
23. M. Mayor, D. Queloz, *Nature* **378**, 355 (1995)
24. See <http://smc.cnes.fr/COROT/>
25. See <http://www.kepler.arc.nasa.gov/>
26. J.J. Fortney, M.S. Marley, J.W. Barnes, *Astrophys. J.* **659**, 1661 (2007)
27. J.J. Fortney, *Contrib. Plasma Phys.* (2013, accepted)
28. See <http://exoplanet.eu/catalog/>
29. W. Borucki, et al., *Science* **327**, 977 (2010)
30. D. Charbonneau, et al., *Nature* **462**, 891 (2009)
31. N. Nettelmann, J. Fortney, U. Kramm, R. Redmer, *Astrophys. J.* **733**, 2 (2011)
32. W. Borucki, et al., *Astrophys. J.* **745**, 120 (2012)
33. J. Lissauer, et al., *Nature* **470**, 53 (2011)
34. T. Barclay, et al., *Nature* **494**, 452 (2013)
35. P. Kalas, J. Graham, M. Camplin, *Nature* **435**, 1067 (2005)
36. J.T. Wright, O. Fakhouri, G.W. Marcy, E. Han, J.A. Feng, Y. and Johnson, D.A. Howard, A. W. and Fischer, J.A. Valenti, J. Anderson, N. Piskunov, *Publ. Astron. Soc. Pac.* **123**, 412 (2011)
37. G. Kresse, J. Hafner, *Phys. Rev. B* **47**, 558 (1993)
38. G. Kresse, J. Hafner, *Phys. Rev. B* **49**, 14251 (1994)
39. G. Kresse, J. Furthmüller, *Phys. Rev. B* **54**, 11169 (1996)
40. L.A. Collins, I. Kwon, J.D. Kress, N.J. Troullier, D. Lynch, *Phys. Rev. E* **52**(6), 6202 (1995)
41. M.W.C. Dharma-wardana, F. Perrot, in *Density Functional Theory*, ed. by E.K.U. Gross, R.M. Dreizler (Plenum Press, New York, 1995), p. 625
42. V. Blum, R. Gehrke, F. Hanke, P. Havu, V. Havu, X. Ren, K. Reuter, M. Scheffler, *Comput. Phys. Commun.* **180**, 2175 (2009)
43. P. Hohenberg, W. Kohn, *Phys. Rev.* **136**, B864 (1964)
44. N.D. Mermin, *Phys. Rev.* **137**, A1441 (1965)
45. P. Haas, F. Tran, P. Blaha, *Phys. Rev. B* **79**, 085104 (2009)
46. W. Kohn, L.J. Sham, *Phys. Rev.* **140**, A1133 (1965)
47. J.P. Perdew, A. Zunger, *Phys. Rev. B* **23**, 5048 (1981)
48. J.P. Perdew, Y. Wang, *Phys. Rev. B* **45**, 13244 (1992)
49. J.P. Perdew, K. Burke, M. Ernzerhof, *Phys. Rev. Lett.* **77**, 3865 (1996)
50. J. Heyd, G.E. Scuseria, M. Ernzerhof, *J. Chem. Phys.* **118**, 8207 (2003)
51. J. Heyd, G.E. Scuseria, M. Ernzerhof, *J. Chem. Phys.* **124**, 219906 (2006)
52. S. Kurth, J.P. Perdew, P. Blaha, *Int. J. Quantum Chem.* **75**, 889 (1999)
53. J. Heyd, G.E. Scuseria, *J. Chem. Phys.* **121**, 1187 (2004)
54. K. Hummer, J. Harl, G. Kresse, *Phys. Rev. B* **80**, 115205 (2009)

55. P. Haas, F. Tran, P. Blaha, L.S. Pedroza, A.J.R. da Silva, M.M. Odashima, K. Capelle, *Phys. Rev. B* **81**, 125136 (2010)
56. P. Söderlind, A. Gonis, *Phys. Rev. B* **82**, 033102 (2010)
57. D.R. Hamann, *Phys. Rev. B* **55**, R10157 (1997)
58. V.N. Staroverov, G.E. Scuseria, J. Tao, J.P. Perdew, *J. Chem. Phys.* **119**, 12129 (2003)
59. J. Heyd, G.E. Scuseria, *J. Chem. Phys.* **120**, 7274 (2004)
60. S.V. Faleev, M. van Schilfgaarde, T. Kotani, F. Léonard, M.P. Desjarlais, *Phys. Rev. B* **74**, 033101 (2006)
61. Y. Zhao, D.G. Truhlar, *J. Chem. Phys.* **130**, 074103 (2009)
62. M. Städele, J.A. Majewski, P. Vogl, A. Görling, *Phys. Rev. Lett.* **79**, 2089 (1997)
63. D.R. Hamann, M. Schlüter, C. Chiang, *Phys. Rev. Lett.* **43**, 1494 (1979)
64. G.B. Bachelet, D.R. Hamann, M. Schlüter, *Phys. Rev. B* **26**, 4199 (1982)
65. D. Vanderbilt, *Phys. Rev. B* **41**, 7892 (1990)
66. G. Kresse, D. Joubert, *Phys. Rev. B* **59**, 1758 (1999)
67. P.E. Blöchl, *Phys. Rev. B* **50**(24), 17953 (1994)
68. H.J. Monkhorst, J.D. Pack, *Phys. Rev. B* **13**, 5188 (1976)
69. A. Baldereschi, *Phys. Rev. B* **7**(12), 5212 (1973)
70. R.P. Feynman, *Phys. Rev.* **56**, 340 (1939)
71. X. Gonze, B. Amadon, P.M. Anglade, J.M. Beuken, F. Bottin, P. Boulanger, F. Bruneval, D. Caliste, R. Caracas, M. Côté, T. Deutsch, L. Genovese, P. Ghosez, M. Giantomassi, S. Goedecker, D. Hamann, P. Hermet, F. Jollet, G. Jomard, S. Leroux, M. Mancini, S. Mazevet, M. Oliveira, G. Onida, Y. Pouillon, T. Rangel, G.M. Rignanese, D. Sangalli, R. Shaltaf, M. Torrent, M. Verstraete, G. Zerah, J. Zwanziger, *Comput. Phys. Commun.* **180**, 2582 (2009)
72. X. Gonze, *Z. Kristallogr.* **220**, 558 (2005)
73. R. Kubo, *J. Phys. Soc. Jap.* **12**, 570 (1957)
74. R. Kubo, M. Yokota, S. Nakajima, *J. Phys. Soc. Jap.* **12**, 1203 (1957)
75. D.A. Greenwood, *Proc. Phys. Soc.* **71**(4), 585 (1958)
76. M.P. Desjarlais, J.D. Kress, L.A. Collins, *Phys. Rev. E* **66**, 025401(R) (2002)
77. S. Mazevet, M. Torrent, V. Recoules, F. Jollet, *High Energy Density Phys.* **6**, 84 (2010)
78. B. Holst, M. French, R. Redmer, *Phys. Rev. B* **83**, 235120 (2011)
79. M. Pozzo, M.P. Desjarlais, D. Alfè, *Phys. Rev. B* **84**, 054203 (2011)
80. S. Mazevet, M.P. Desjarlais, L.A. Collins, J.D. Kress, N.H. Magee, *Phys. Rev. E* **71**, 016409 (2005)
81. M. French, T.R. Mattsson, R. Redmer, *Phys. Rev. B* **82**, 174108 (2010)
82. M. French, S. Hamel, R. Redmer, *Phys. Rev. Lett.* **107**, 185901 (2011)
83. B. Holst, R. Redmer, M.P. Desjarlais, *Phys. Rev. B* **77**(18), 184201 (2008)
84. L. Caillabet, S. Mazevet, P. Loubeyre, *Phys. Rev. B* **83**, 094101 (2011)
85. J.M. McMahon, M.A. Morales, C. Pierleoni, D.M. Ceperley, *Rev. Mod. Phys.* **84**, 1607 (2012)
86. M.A. Morales, C. Pierleoni, E. Schwegler, D.M. Ceperley, *Proc. Natl. Acad. Sci. USA* **107**, 12799 (2010)
87. W. Lorenzen, B. Holst, R. Redmer, *Phys. Rev. B* **82**, 195107 (2010)
88. V. Dzyabura, M. Zaghoo, I. Silvera, *PNAS* **110**, 8040 (2013)
89. N. Nettelmann, A. Becker, B. Holst, R. Redmer, *Astrophys. J.* **750**, 52 (2012)
90. I. Tamblyn, S.A. Bonev, *Phys. Rev. Lett.* **104**(6), 065702 (2010)
91. M.A. Morales, J.M. McMahon, C. Pierleoni, D.M. Ceperley, *Phys. Rev. Lett.* **110**, 065702 (2013)
92. J. Vorberger, I. Tamblyn, B. Militzer, S.A. Bonev, *Phys. Rev. B* **75**, 024206 (2007)
93. B. Militzer, *Phys. Rev. B* **79**, 014202 (2013)
94. M.A. Morales, E. Schwegler, D. Ceperley, C. Pierleoni, S. Hamel, K. Caspersen, *Proc. Natl. Acad. Sci. USA* **106**(5), 1324 (2009)
95. N. Nettelmann, B. Holst, A. Kietzmann, M. French, R. Redmer, D. Blaschke, *Astrophys. J.* **683**(2), 1217 (2008)
96. W. Lorenzen, B. Holst, R. Redmer, *Phys. Rev. B* **84**, 235109 (2011)

97. V.V. Kechin, *J. Phys.: Condens. Matter* **7**, 531 (1995)
98. R.K. Crawford, W.B. Daniels, *J. Chem. Phys.* **55**, 5651 (1971)
99. R.L. Mills, D.H. Liebenberg, J.C. Bronson, *Phys. Rev. B* **21**, 5137 (1980)
100. W.L. Vos, M.G.E. van Hinsberg, J.A. Schouten, *Phys. Rev. B* **42**, 6106 (1990)
101. F. Datchi, P. Loubeyre, R. Le Toullec, *Phys. Rev. B* **61**, 6535 (2000)
102. D. Santamaría-Pérez, G.D. Mukherjee, B. Schwager, R. Boehler, *Phys. Rev. B* **81**, 214101 (2010)
103. W. Lorenzen, B. Holst, R. Redmer, *Phys. Rev. Lett.* **102**, 115701 (2009)
104. M.A. Morales, S. Hamel, K. Caspersen, E. Schwegler, *Phys. Rev. B* **87**, 174105 (2013)
105. J.E. Klepeis, K.J. Schafer, T.W. Barbee, M. Ross, *Science* **254**, 986 (1991)
106. O. Pfaffenzeller, D. Hohl, P. Ballone, *Phys. Rev. Lett.* **74**, 2599 (1995)
107. P.M. Celliers, G.W. Collins, L.B. DaSilva, D.M. Gold, R. Cauble, R.J. Wallace, M.E. Foord, B.A. Hammel, *Phys. Rev. Lett.* **84**, 5564 (2000)
108. T. Sano, N. Ozaki, T. Sakaiya, K. Shigemori, M. Ikoma, T. Kimura, K. Miyanishi, T. Endo, A. Shiroshita, H. Takahashi, T. Jitsui, Y. Hori, Y. Hironaka, A. Iwamoto, T. Kadono, M. Nakai, T. Okuchi, K. Otani, K. Shimizu, T. Kondo, R. Kodama, K. Mima, *Phys. Rev. B* **83**, 054117 (2011)
109. S.T. Weir, A.C. Mitchell, W.J. Nellis, *Phys. Rev. Lett.* **76**, 1860 (1996)
110. W.J. Nellis, *Rep. Prog. Phys.* **69**, 1479 (2006)
111. M.D. Knudson, D.L. Hanson, J.E. Bailey, C.A. Hall, J.R. Asay, C. Deeney, *Phys. Rev. B* **69**, 144209 (2004)
112. M.D. Knudson, M.P. Desjarlais, D.H. Dolan, *Science* **322**, 1822 (2008)
113. V.E. Fortov, V.Y. Ternovoi, M.V. Zhernokletov, M.A. Mochalov, A.L. Mikhailov, A.S. Filimonov, A.A. Pyalling, V.B. Mintsev, V.K. Gryaznov, I.L. Iosilevskii, *J. Exp. Theor. Phys.* **97**, 259 (2003)
114. G.V. Boriskov, A.I. Bykov, R.I. Il'kaev, V.D. Selemir, G.V. Simakov, R.F. Trunin, V.D. Urlin, A.N. Shuikin, W.J. Nellis, *Phys. Rev. B* **71**, 092104 (2005)
115. M.D. Knudson, D.L. Hanson, J.E. Bailey, C.A. Hall, J.R. Asay, W.W. Anderson, *Phys. Rev. Lett.* **87**, 225501 (2001)
116. M.D. Knudson, D.L. Hanson, J.E. Bailey, C.A. Hall, J.R. Asay, *Phys. Rev. Lett.* **90**, 035505 (2003)
117. P. Loubeyre, S. Brygoo, J. Eggert, P.M. Celliers, D.K. Spaulding, J.R. Rygg, T.R. Boehly, G.W. Collins, R. Jeanloz, *Phys. Rev. B* **86**, 144115 (2012)
118. V.E. Fortov, R.I. Ilkaev, V.A. Arinin, V.V. Burtzev, V.A. Golubev, I.L. Iosilevskiy, V.V. Khrustalev, A.L. Mikhailov, M.A. Mochalov, V.Y. Ternovoi, M.V. Zhernokletov, *Phys. Rev. Lett.* **99**(18), 185001 (2007)
119. M. Mochalov, R. Il'kaev, V. Fortov, A. Mikhailov, Y. Makarov, V. Arinin, S. Grishechkin, A. Blikov, V. Ogorodnikov, A. Ryzhkov, V. Gryaznov, *JETP Lett.* **92**, 300 (2010)
120. A. Becker, N. Nettelmann, B. Holst, R. Redmer, *Phys. Rev. B* **88**, 045122 (2013)
121. B. Holst, R. Redmer, V. Gryaznov, V. Fortov, I. Iosilevskiy, *Eur. Phys. J. D* **66**, 1 (2012)
122. B. Militzer, *Phys. Rev. Lett.* **97**, 175501 (2006)
123. W.B. Hubbard, W.J. Nellis, A.C. Mitchell, N.C. Holmes, S.S. Limaye, P.C. MacCandless, *Science* **253**, 648 (1991)
124. C. Cavazzoni, G.L. Chiarotti, S. Scandolo, E. Tosatti, M. Bernasconi, M. Parrinello, *Science* **283**, 44 (1999)
125. M. French, T.R. Mattsson, N. Nettelmann, R. Redmer, *Phys. Rev. B* **79**, 054107 (2009)
126. M.D. Knudson, M.P. Desjarlais, R.W. Lemke, T.R. Mattsson, M. French, N. Nettelmann, R. Redmer, *Phys. Rev. Lett.* **108**, 091102 (2012)
127. N. Ozaki, T. Kimura, T. Okuchi, M. French, T. Kakeshita, M. Kita, K. Miyanishi, R. Redmer, T. Sano, T. Sano, K. Shimizu, T. Terai, R. Kodama (submitted)
128. A.C. Mitchell, W.J. Nellis, *J. Chem. Phys.* **76**, 6273 (1982)
129. L. Volkov, et al., *JETP Letters* **31**, 513 (1980)
130. P.M. Celliers, G.W. Collins, D.G. Hicks, M. Koenig, E. Henry, A. Benuzzi-Mounaix, D. Batani, D.K. Bradley, L.B.D. Silva, R.J. Wallace, S.J. Moon, J.H. Eggert, K.K.M. Lee, L.R.

- Benedetti, R. Jeanloz, I.M.N. Dague, B. Marchet, M.R.L. Gloahec, C. Reverdin, J. Pasley, O. Willi, D. Neely, C. Danson, *Phys. Plasmas* **11**(8), L41 (2004)
131. M. French, R. Redmer, *J. Phys. Condens. Matter* **21**, 375101 (2009)
132. M. Podurets, et al., *Sov. Phys. JETP* **35**, 375 (1972)
133. N. Nettelmann, R. Helled, J. Fortney, R. Redmer, *Planet. Space Sci.* **77**, 143 (2013)
134. H.B. Radousky, A.C. Mitchell, W.J. Nellis, *J. Chem. Phys.* **93**, 8235 (1990)
135. W.J. Nellis, N.C. Holmes, A.C. Mitchell, D.C. Hamilton, M. Nicol, *J. Chem. Phys.* **107**(21), 9096 (1997)
136. F. Datchi, S. Ninet, M. Gauthier, A.M. Saitta, B. Canny, F. Decremps, *Phys. Rev. B* **73**, 174111 (2006)
137. C.J. Pickard, R.J. Needs, *Nat. Mater.* **7**, 775 (2008)
138. G.I.G. Griffiths, R.J. Needs, C.J. Pickard, *Phys. Rev. B* **86**, 144102 (2012)
139. S. Ninet, F. Datchi, A.M. Saitta, *Phys. Rev. Lett.* **108**, 165702 (2012)
140. J.G.O. Ojwang, R.S. McWilliams, X. Ke, A.F. Goncharov, *J. Chem. Phys.* **137**, 064507 (2012)
141. M. Bethkenhagen, M. French, R. Redmer, *J. Chem. Phys.* **138**, 234504 (2013)
142. L.R. Benedetti, J.H. Nguyen, W.A. Caldwell, H. Liu, M. Kruger, R. Jeanloz, *Science* **286**(5437), 100 (1999)
143. G. Gao, A.R. Oganov, Y. Ma, H. Wang, P. Li, Y. Li, T. Iitaka, G. Zou, *J. Chem. Phys.* **133**(14), 144508 (2010)
144. B.L. Sherman, H.F. Wilson, D. Weeraratne, B. Militzer, *Phys. Rev. B* **86**, 224113 (2012)
145. R. Chau, S. Hamel, W.J. Nellis, *Nat. Commun.* **2**, 203 (2011)
146. M.S. Lee, S. Scandolo, *Nat. Commun.* **2**, 185 (2011)
147. F.D. Stacey, *Rep. Prog. Phys.* **68**, 341 (2006)
148. A.R. Oganov, G.D. Price, S. Scandolo, *Z. Kristallogr.* **220**, 531 (2005)
149. M.J. Gillan, D. Alfè, J. Brodholt, L. Vočadlo, G.D. Price, *Rep. Prog. Phys.* **69**, 2365 (2006)
150. R.J. Hemley, *High Press. Res.* **30**, 581 (2010)
151. L. Stixrude, N. de Koker, N. Sun, M. Mookherjee, B.B. Karki, *Earth Planet. Sci. Lett.* **278**, 226 (2009)
152. N. de Koker, L. Stixrude, *Geophys. J. Int.* **178**, 162 (2009)
153. D.K. Spaulding, R.S. McWilliams, R. Jeanloz, J.H. Eggert, P.M. Celliers, D.G. Hicks, G.W. Collins, R.F. Smith, *Phys. Rev. Lett.* **108**, 065701 (2012)
154. D.C. Swift, J.H. Eggert, D.G. Hicks, S. Hamel, K. Caspersen, E. Schwegler, G.W. Collins, N. Nettelmann, G.J. Ackland, *Astrophys. J.* **744**(1), 59 (2012)
155. D. Valencia, M. Ikoma, T. Guillot, N. Nettelmann, *Astron. Astrophys.* **516**, A20 (2010)
156. L. Stixrude, *Phys. Rev. Lett.* **108**, 055505 (2012)
157. D. Alfè, M.J. Gillan, G.D. Price, *Nature* **401**, 462 (1999)
158. E. Sola, D. Alfè, *Phys. Rev. Lett.* **103**, 078501 (2009)
159. D. Alfè, M. Pozzo, M.P. Desjarlais, *Phys. Rev. B* **85**, 024102 (2012)
160. N. de Koker, G. Steinle-Neumann, V. Vlcek, *Proc. Natl. Acad. Sci.* **109**, 470 (2012)
161. D. Valencia, R.J. O'Connell, D. Sasselo, *Icarus* **181**, 545 (2006)
162. L.A. Rogers, P. Bodenheimer, J.J. Lissauer, S. Seager, *Astrophys. J.* **738**, 59 (2011)
163. V. Stamenkovic, D. Breuer, T. Spohn, *Icarus* **216**, 572 (2011)
164. V. Zharkov, A. Makalkin, V. Trubitsyn, *Astron. Zh.* **51**, 1288 (1974)
165. W.B. Hubbard, M.S. Marley, *Icarus* **78**, 102 (1989)
166. G. Chabrier, D. Saumon, W.B. Hubbard, J.I. Lunine, *Astrophys. J.* **391**, 817 (1992)
167. T. Gudkova, V. Zharkov, *Planet. Space Sci.* **47**, 1201 (1999)
168. T. Guillot, *Planet. Space Sci.* **47**, 1183 (1999)
169. B. Militzer, W.B. Hubbard, J. Vorberger, I. Tamblyn, S.A. Bonev, *Astrophys. J. Lett.* **688**, L45 (2008)
170. N. Nettelmann, *Astrophys. Space Sci.* **336**, 47 (2011)
171. J. Leconte, G. Chabrier, *Astron. Astrophys.* **540**, A20 (2012)
172. J. Lissauer, *Annu. Rev. Astron. Astrophys.* **31**, 129 (1993)
173. J. Pollack, O. Hubickyj, P. Bodenheimer, J. Lissauer, M. Podolak, Y. Greenzweig, *Icarus* **124**, 62 (1996)

174. L. Mayer, T. Quinn, J. Wadsley, J. Stadel, *Science* **298**, 5599 (2002)
175. A.P. Boss, *Astrophys. J.* **599**, 577 (2003)
176. R. Helled, T. Guillot, *Astrophys. J.* **767**, 113 (2013)
177. N. Nettelmann, R. Püster, R. Redmer, *Icarus* **225**, 548 (2013)
178. D. Saumon, G. Chabrier, H.M. van Horn, *Astrophys. J. Suppl. Ser.* **99**, 713 (1995)
179. S. Lyon, J. Johnson, Sesame, Technical report, Los Alamos National Laboratory Equation of State Database. LANL report no. LA-UR-92-3407 (1992)
180. G.I. Kerley, Structures of the planets jupiter and saturn. Kerley Technical Services Research Report KTS04-1, Kerley Technical Services (2004)
181. D. Saumon, T. Guillot, *Astrophys. J.* **609**, 1170 (2004)
182. B. Militzer, W.B. Hubbard, *Astrophys. J.* **773**, 95 (2013)
183. J. Liu, P. Goldreich, D. Stevenson, *Icarus* **196**, 653 (2008)
184. W.J. Nellis, A.C. Mitchell, P.C. McCandless, D.J. Erskine, S.T. Weir, *Phys. Rev. Lett.* **68**, 2937 (1992)
185. W.J. Nellis, S.T. Weir, A.C. Mitchell, *Science* **273**(5277), 936 (1996)
186. M. French, A. Becker, W. Lorenzen, N. Nettelmann, M. Bethkenhagen, J. Wicht, R. Redmer, *Astrophys. J. Suppl. Ser.* **202**, 5 (2012)
187. N. Gómez-Pérez, M. Heimpel, J. Wicht, *Phys. Earth Planet. Inter.* **181**, 42 (2010)
188. R. Helled, J. Anderson, M. Podolak, G. Schubert, *Astrophys. J.* **726**, A15 (2011)
189. S. Stanley, J. Bloxham, *Nature* **428**, 151 (2004)
190. S. Stanley, J. Bloxham, *Icarus* **184**, 556 (2006)
191. D.J. Stevenson, E.E. Salpeter, *Astrophys. J. Suppl. Ser.* **35**, 221 (1977)
192. G. Chabrier, I. Baraffe, *Astrophys. J.* **661**, L81 (2007)
193. W. Hubbard, *Astrophys. J.* **162**, 687 (1970)
194. D. Saumon, G. Chabrier, *Phys. Rev. A* **46**, 2084 (1992)
195. T. Guillot, G. Chabrier, D. Gautier, P. Morel, *ApJ* **450**, 463 (1995)
196. J.J. Fortney, W.B. Hubbard, *Icarus* **164**, 228 (2003)
197. W. Hubbard, *Icarus* **30**, 305 (1977)
198. N. Nettelmann, Matter under extreme conditions: modelling giant planets. PhD thesis, University of Rostock (2009)
199. U. von Zahn, D.M. Hunten, G. Lehman, *J. Geophys. Res.* **103**, 0148 (1998)
200. B.J. Conrath, D. Gautier, *Icarus* **144**, 124 (2000)
201. J. Leconte, G. Chabrier, *Nat. Geosci.* **6**, 347 (2013)
202. W.B. Hubbard, H.E. DeWitt, *Astrophys. J.* **290**, 388 (1985)
203. J.J. Fortney, W.B. Hubbard, *Astrophys. J.* **608**(2, Part 1), 1039 (2004)



Frontiers and Challenges in Warm Dense Matter

Graziani, F.; Desjarlais, M.P.; Redmer, R.; Trickey, S.B.  
(Eds.)

2014, X, 282 p. 89 illus., 64 illus. in color., Hardcover

ISBN: 978-3-319-04911-3